Quaternary Geochronology 45 (2018) 37–49

Contents lists available at ScienceDirect

Quaternary Geochronology

journal homepage: www.elsevier.com/locate/quageo

Research paper

Single-grain feldspar luminescence chronology of historical extreme wave event deposits recorded in a coastal lowland, Pacific coast of central Japan

Svenja Riedesel[a,b,*], Dominik Brill[a], Helen M. Roberts[b], Geoff A.T. Duller[b], Ed Garrett[c,d], Anja M. Zander[a], Georgina E. King[e], Toru Tamura[f], Christoph Burow[a], Alastair Cunningham[g,h], Martin Seeliger[a], Marc De Batist[i], Vanessa M.A. Heyvaert[d], Osamu Fujiwara[f], Helmut Brückner[a], the QuakeRecNankai Team[1]

[a] Institute of Geography, University of Cologne, Germany
[b] Department of Geography and Earth Sciences, Aberystwyth University, United Kingdom
[c] Department of Geography, Durham University, United Kingdom
[d] Geological Survey of Belgium, Brussels, Belgium
[e] Institute of Geological Sciences and Oeschger Centre for Climate Change Research, University of Bern, Switzerland
[f] Geological Survey of Japan, AIST, Japan
[g] Department of Geoscience, Aarhus University, DTU Nutech, Risø Campus, DK-4000, Roskilde, Denmark
[h] Center for Nuclear Technologies, Technical University of Denmark, DTU Risø Campus, DK-4000, Roskilde, Denmark
[i] Department of Geology, Ghent University, Belgium

ARTICLE INFO

Keywords:
Feldspar
Single-grain dating
$IRSL_{50}$
Low temperature post-IR IRSL
Tsunami

ABSTRACT

The Shirasuka lowlands, located on the Enshu-nada coast of central Japan, record evidence for numerous extreme wave events. Here we test the applicability of using the luminescence signal from feldspars to date these young (< 1000 a) extreme wave event deposits. The signal used for dating is the IRSL signal (measured at 50 °C) as part of a post-IR $IRSL_{130}$ procedure. We demonstrate that this $IRSL_{50}$ (pre-IR_{130}) signal results in reliable ages when corrected for fading, and the post-IR $IRSL_{130}$ stimulation functions as an optical wash for both the natural/regenerated luminescence signal (L_x) and the test dose signal (T_x), lowering the recuperation and removing any remaining charge from previous steps in the protocol. The single grain $IRSL_{50}$ (pre-IR_{130}) ages generated cover the historical record of the past 800 years and correlate well with past earthquakes and tsunamis in 1361 CE, 1498 CE and 1605 CE. Another identified tsunami deposit may correlate with the 1707 CE earthquake and tsunami. A slope failure deposit, probably caused by the earthquake in 1944 CE, is also identified. This study demonstrates that accurate ages can be determined for the young, extreme wave events at this site using the luminescence signal from feldspars.

1. Introduction

The Indian Ocean Tsunami in 2004 and the Tōhoku-oki Tsunami in 2011 caused dramatic damage to coastal settlements and thousands of casualties, drawing the attention of the public and scientists to the impact and history of tsunamis. Since then, numerous studies have developed approaches to identify the characteristics, impact and age of tsunami deposits (e.g. Dawson and Stewart, 2007; Jankaew et al., 2008; Monecke et al., 2008; Engel et al., 2010; Switzer et al., 2012; May et al., 2016). Storm surges, another major threat to coastal communities, are also the focus of research due to recent disasters like Typhoon Haiyan, which hit the Philippine coast in 2013 (e.g. Brill et al., 2016; Pilarczyk et al., 2016; Soria et al., 2017). Studies observing proxies and characteristics of extreme wave event deposits contribute to improvements in their identification in the geological record (e.g. Morton et al., 2007; Chagué-Goff et al., 2011; Shanmugam, 2012), while chronological studies of past extreme wave events enable the identification of recurrence intervals, intensities and past impacts (Brill et al., 2012a; Prendergast et al., 2012).

The Shirasuka lowlands in central Japan record evidence for numerous extreme wave events, as previously demonstrated by Fujiwara et al. (2006), Komatsubara et al. (2008) and Garrett et al. (in press). The sedimentary record of extreme wave event deposits of the Shirasuka lowlands has been constrained by radiocarbon dating to be younger

* Corresponding author. Department of Geography and Earth Sciences, Aberystwyth University, Aberystwyth, SY23 3DB, United Kingdom.
E-mail addresses: svr1@aber.ac.uk, riedeselsvenja@gmail.com (S. Riedesel).
[1] List of members available from http://www.quakerecnankai.ugent.be/index.php?team.

https://doi.org/10.1016/j.quageo.2018.01.006
Received 5 August 2017; Received in revised form 23 January 2018; Accepted 29 January 2018
Available online 31 January 2018
1871-1014/

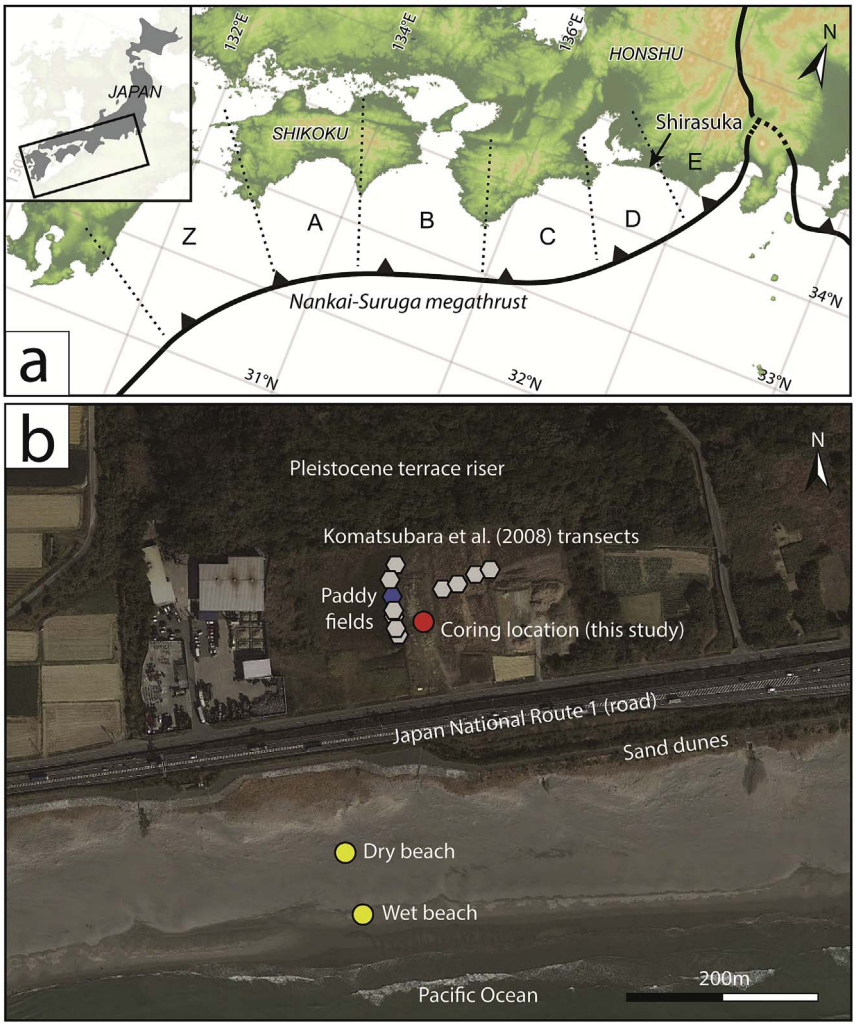

Fig. 1. Geographical and tectonic setting of the Shirasuka lowlands. (a) Geographical location of the broader study area, tectonic situation and geographical position of the Shirasuka lowlands (source: GeoMapApp (http://www.geomapapp.org); (b) sampling locations of modern beach sediments (JSH-MOD3 from the wet beach, and JSH–MOD4 from the dry beach) and the various sediment cores discussed in the text (source: Google Earth, Terra Metrics, image taken on 27th February 2017).

than 1200 CE (Fujiwara et al., 2006; Komatsubara et al., 2008). From 12th century CE onwards, at least six megathrust earthquakes and subsequent tsunamis occurred in the eastern segments (C and D) of the Nankai Trough (Ando, 1975, Fig. 1). The region also has a long historical record of earthquakes and subsequent tsunamis from 684 CE onwards, captured in a range of sources such as chronicles (e.g. *Nihon Shoki*), reports, and governmental records (e.g. Ando, 1975; Usami, 1979; Ishibashi, 2004; Goff et al., 2016). However, there are several issues which have complicated previous efforts to reconstruct the local record of past extreme wave events based on the study of the sedimentary evidence preserved at Shirasuka: (1) The lowlands provide a complex stratigraphy with laterally discontinuous event layers, which complicates stratigraphic correlations between sediment cores (Fujiwara et al., 2006; Komatsubara et al., 2008; Garrett et al., in press), and makes chronology essential to correlate different core records; (2) the lack of material appropriate for radiocarbon dating often means that this method cannot always be used to determine ages where they are needed; (3) even where material suitable for radiocarbon dating exists, a plateau in the radiocarbon calibration curve prevents the establishment of a high-resolution chronostratigraphy during the time period of interest (Stuiver, 1978; Madsen et al., 2009).

Unlike radiocarbon dating, optically stimulated luminescence (OSL) techniques do not typically suffer from a lack of suitable material for dating as they rely upon use of one of the two most abundant minerals on Earth, quartz or feldspars. A further advantage of OSL is that the sediments used for dating directly record the age of the deposition event, e.g. the burial age of a tsunami event layer (e.g. Brill et al., 2012a, b). However, whilst the use of OSL has previously been explored in a range of extreme wave event settings (Huntley and Clague, 1996; Murari et al., 2007; Cunha et al., 2010; Brill et al., 2012a, b; Prendergast et al., 2012; Spiske et al., 2013; Tamura et al., 2015), issues still persist. Firstly, incomplete resetting of the luminescence signal during tsunami or storm surge transport, prior to deposition of the sediments, needs to be considered (e.g. Madsen and Murray, 2009). The fast component of the OSL signal from quartz bleaches more rapidly than any other luminescence signal routinely used for dating, and this makes it the preferred mineral for dating young and potentially incompletely-bleached sediments (e.g. Bishop et al., 2005; Murari et al., 2007; Cunningham et al., 2011; Brill et al., 2012a, b; Li et al., 2017). However, previous studies of quartz OSL in tectonically active regions have shown challenging luminescence properties (e.g. Tsukamoto et al., 2003; Kondo et al., 2007; Steffen et al., 2009; Neudorf et al., 2015; Tamura et al., 2015). Thus, OSL of feldspars may provide a useful alternative chronometer if they can be demonstrated to be suitable for dating very young (< 1000 years), and potentially incompletely-bleached sediments.

The OSL signal from feldspar bleaches more slowly than that of quartz (e.g. Buylaert et al., 2012; Colarossi et al., 2015), and suffers from an athermal signal loss called anomalous fading (Wintle, 1973), which can result in age under-estimations. Low-temperature post-

infrared infrared stimulated luminescence (post-IR IRSL) dating offers a promising approach for dating young deposits using feldspars (e.g. Madsen et al., 2011; Reimann and Tsukamoto, 2012), since it may minimise anomalous fading whilst still accessing signals that are adequately bleached for dating (Kars et al., 2014). However, it should be noted that previous applications were to dune and beach deposits, where the opportunity for exposure to daylight prior to deposition is much greater than may be the case for high magnitude events such as a tsunami.

In this study we aim to test the suitability of optically stimulated luminescence (OSL) techniques to provide a chronology for young (< 1000 years) extreme wave event deposits in the Shirasuka lowlands of tectonically active central Japan. If successful, OSL may help refine the record of extreme wave events preserved at both Shirasuka and elsewhere.

2. Field site

2.1. Study area and existing chronostratigraphy

The Japanese islands are situated at two triple junctions of tectonic plates. South of the main island of Honshu, the Philippine Sea Plate subducts beneath the Eurasian Plate at a rate of approximately 40–55 mm/a (Mazzotti et al., 2000; Loveless and Meade, 2010). The subduction zone is subdivided into six segments (Fig. 1a), which have ruptured during twelve historically documented multi-segment megathrust earthquakes (> M8) since 684 CE (Ando, 1975; Satake, 2015; Garrett et al., 2016). The study area of Shirasuka (Fig. 1b) is located close to the approximate boundary of segments D and E (Fig. 1a).

Sandwiched between a ~60–80 m high mid-Pleistocene terrace and a ~10 m high coastal dune (height artificially increased in the early 21st century, because of the construction of the Shiomi By-pass of Japan National Route 1), the marshy coastal lowlands of Shirasuka are ideally situated to record evidence of typhoons and tsunamis (Fig. 1b). Sediment cores from the lowlands are mainly composed of fine-grained marsh deposits intercalated with sand-rich layers (Fujiwara et al., 2006; Komatsubara et al., 2008; Garrett et al., in press; Fig. 2). Komatsubara et al. (2008) obtained a set of cores (hexagonal symbols on Fig. 1b) from these lowlands and used 21 radiocarbon ages to generate a chronology for them which covers the timespan from ~1200 CE onwards. The cores include sand layers interpreted as resulting from tsunamis and storm surges as well as slope failures (event deposits A to G in ascending order, according to Komatsubara et al., 2008). Komatsubara et al. (2008) tentatively correlate the sand layers B, C, E and F in their cores with the 1498 CE Meiō, 1605 Keichō, 1707 Hōei and 1854 CE Ansei-Tōnankai events where both an earthquake and a tsunami are recorded. Given the excellent historical record of extreme wave events available for this region, this study site provides an ideal opportunity to assess whether luminescence dating can provide accurate ages for extreme wave events.

2.2. Fieldwork and sampling strategy

Two overlapping sediment cores taken ~0.5 m apart (JSH1b/full, JSH1/overlap; Figs. 1 and 2) were recovered by vibra coring (Atlas Copco Cobra TT) using closed steel auger heads and opaque 50 mm diameter PVC tubes. Sediment cores were opened in the laboratory under subdued red light. The sediment cores consist of clayey-silty deposits with intercalated sand layers. The lower contact of the sand layers is aprupt and the sand includes clay lenses (rip-up clasts) and mud caps. This suggests rapid high-energy erosional processes. We interpret the sand layers to be either tsunami or storm surge deposits. The stratigraphy for both sediment cores is shown in Fig. 2 and described in detail in Garrett et al. (in press). Sand layers were sampled for luminescence dating and dosimetry. Where the stratigraphy changed within 30 cm of an OSL sample, additional dosimetry samples were taken from the differing sedimentary units within 30 cm distance from the OSL sample, to adequately assess the dose rate to that OSL sample. In total, 10 samples were dated by OSL (Fig. 2), the dose rate was determined for 18 samples (Fig. 2; Table S1). In addition, two modern samples (Fig. 1b) were collected from the beach by hammering opaque plastic tubes in the sand, approximately 2–3 cm below the surface.

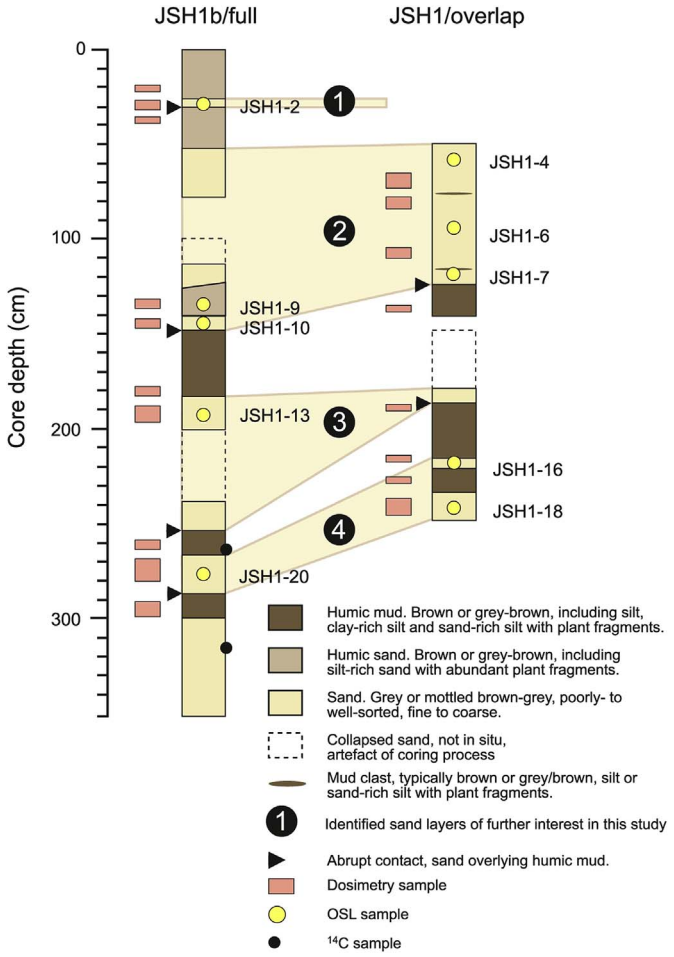

Fig. 2. Sediment cores JSH1b/full and JSH1/overlap taken for this study. Four sand layers (labelled 1 to 4) are observed, and units 2, 3 and 4 can be correlated between the two cores. Location of dosimetry, OSL and radiocarbon samples (from Garrett et al., in press) in the cores are given.

3. Luminescence dating

3.1. Sample preparation

Luminescence samples were prepared under subdued red light in the Cologne Luminescence Laboratory (CLL). Prior to palaeodose determination, hydrochloric acid (HCl; 10%), hydrogen peroxide (H_2O_2; 10%) and sodium oxalate ($Na_2C_2O_4$; 0.01 N) were used to remove carbonates, organic matter and to disperse the particles. Samples were dry sieved to separate the 100–200 µm fraction that was then density separated using sodium polytungstate to isolate quartz (2.68 g/cm^3 > ρ > 2.62 g/cm^3) and alkali-feldspar fractions (ρ < 2.58 g/cm^3). The quartz fraction was etched with concentrated hydrofluoric acid (40%) for 40 min and subsequently treated with HCl (10%) to remove any fluorides. Subsequent tests of the quartz material suggested that, in accordance with other studies on Japanese quartz (e.g. Tsukamoto et al., 2003; Tamura et al., 2015), the material shows inappropriate luminescence properties, which are unsuitable for quartz OSL dating. Hence, quartz is not considered further in the manuscript,

although the main characteristics are outlined in Supplementary Information.

Multiple-grain aliquot (MG) measurements were made at the CLL, using grains mounted on stainless steel discs and fixed using a 1 mm patch of silicone oil. Single-grain (SG) measurements were made at the Aberystwyth Luminescence Research Laboratory (ALRL), using 100–200 μm grains brushed into the 300 μm diameter holes of standard single-grain discs. The size-range of the sieved fraction may cause the presence of more than one grain within one hole; this was checked on a random basis and was found to occur only very occasionally.

3.2. Dosimetry

Uranium (U), Thorium (Th) and Potassium (K) contents were determined by high-resolution gamma spectrometry in the CLL. Approximately 200 g of dried, homogenised sediment was stored in an airtight box for at least four weeks to compensate for radon loss induced by sample preparation, before measurement with an Ortec Profile M-Series GEM Coaxial P-type high-precision Germanium Gamma-Ray detector. For eight samples (JSH1-2Dn, JSH1-6Dn-7Dn, JSH1-10Dn, and JSH1-16Dn to JSH1-20Dn), only very small amounts of sediment were available; these were measured at VKTA Dresden using low-level-gamma spectrometry (Table S1).

To measure the potassium content of the alkali-feldspar separates, 100 mg of each sample was analysed on a Risø GM-25-5 beta counter. An average internal K-content of 6.44 ± 1.05% was measured (Table 1) but a K-content of 10 ± 2% was used to calculate the dose rate used in combination with equivalent doses (D_e) from single grains, assuming that the grains with higher K-content have a brighter IRSL signal and are more likely to generate a D_e (Smedley et al., 2012).

The stratigraphy of the Shirasuka lowlands is complex and shows abrupt changes in grain size, which may cause variations in the gamma dose rate. Layer-to-layer variations in gamma dose rate were calculated according to Aitken (1985, Appendix H), using the multi-layer gamma spreadsheet of Ian Bailiff, Durham University (personal communication) to give the gamma dose rate values shown in Table 1. DRAC v1.1 (Durcan et al., 2015) was used to calculate internal and external alpha and beta dose rates, and to correct them for water content. Conversion factors for gamma and beta dose rates are based on Adamiec and Aitken (1998). Alpha and beta grain size attenuation factors of Bell (1980) and Guerin et al. (2012, for feldspars), respectively, were applied. Alpha efficiency was determined for samples JSH1-4 and JSH1-10, and gave values of 0.072 ± 0.003 for the $IRSL_{50}$ (pre-IR_{130}) signal, and 0.095 ± 0.008 for the post-IR $IRSL_{130}$ signal (see Supplementary Information for further details). The cosmic dose rate was determined in accordance with Prescott and Hutton (1994). Information on dose rates (Gy/ka) calculated for each sample in this study are given in Table 1.

3.3. Instrumentation and methods for feldspar measurements

Luminescence measurements were made using single-aliquot regenerative dose (SAR) protocols on Risø TL/OSL readers equipped with $^{90}Sr/^{90}Y$ beta sources delivering dose rates of ~0.0837 Gy/s, ~0.0760 Gy/s and ~0.0366 Gy/s, depending on the instrument.

Two sets of OSL measurements were made on feldspars. Small (1 mm diameter), multiple-grain aliquots were measured at the CLL, stimulated using IR LEDs (870 nm, FWHM 40 nm) and detected through a D410/30x LOT interference filter. Single-grain equivalent dose measurements were performed at ALRL using an IR laser (830 nm, 150 mW, with a Schott RG-780 filter in front of the laser to remove emission below 780 nm) and detected using a combination of 4.1 mm BG-39 and 2.1 mm Corning 7–59 glass filters. A convex quartz lens was used to maximise the signal collection efficiency during single grain measurements.

All feldspar single-aliquot and single-grain datasets with recycling ratios and test dose uncertainties within 10% were accepted for palaeodose calculations (see section 4 for details of the measurement protocols considered). Fading measurements were conducted according to Auclair et al. (2003). The samples were bleached for 24 h in a Hönle SOL2 solar simulator and subsequently irradiated to ~23 Gy. The shortest delay between the start of an irradiation and the start of a measurement was 218 s, the longest 18,000 s. Ages were corrected for fading using the correction model of Huntley and Lamothe (2001) implemented in the R-package 'Luminescence' (Kreutzer et al., 2012; Kreutzer, 2016).

4. Measurement protocols for feldspar

Inappropriate luminescence properties of the quartz in this study means that reliable signals cannot be obtained for quartz OSL dating (see Supplementary Information). Measurement protocols using infrared stimulated luminescence (IRSL) signals from feldspar were therefore investigated, using multiple-grain aliquots of coarse-grain feldspar to examine the signal behaviour and identify the most appropriate

Table 1
U, Th and K concentrations derived from high resolution gamma spectrometry, measured water content, internal K content derived from beta counting, and values of the cosmic dose rate derived from the burial depth and geographical position of the coring location. The gamma dose rate given here was calculated using all layers influencing the luminescence samples, according to Aitken (1985).

Sample[a]	Lab Code	Core	Depth (cm)	U (ppm)	Th (ppm)	K (%)	Water content (%) [b]	Internal K [c]	Multi-layer gamma dose rate (Gy/ka)	Cosmic dose rate (Gy/ka)	Environmental dose rate (Gy/ka)[d]
JSH1-2	C-L3944	JSH1b-full	47–53	2.30 ± 0.40	18.2 ± 1.2	1.72 ± 0.13	13.9	8.23 ± 0.44	1.28 ± 0.15	0.20 ± 0.02	3.83 ± 0.31
JSH1-4	C-L3946	JSH1 OL	77–82	2.25 ± 0.14	25.4 ± 1.5	1.57 ± 0.02	28.2	7.78 ± 052	1.57 ± 0.13	0.19 ± 0.02	3.92 ± 0.26
JSH1-6	C-L3948	JSH1 OL	112–117	2.70 ± 0.40[e]	32.6 ± 2.0[e]	1.57 ± 0.13[e]	22.6	n.d.	1.41 ± 0.18	0.18 ± 0.02	4.06 ± 0.33
JSH1-7	C-L3949	JSH1 OL	125–134				30.0	6.24 ± 0.58	1.39 ± 0.16	0.17 ± 0.02	3.91 ± 0.3
JSH1-9	C-L3951	JSH1b-full	133–137	2.14 ± 0.13	31.2 ± 1.8	1.47 ± 0.02	34.6	6.84 ± 0.26	1.52 ± 0.14	0.17 ± 0.02	3.82 ± 0.26
JSH1-10	C-L3952	JSH1b-full	144–146	2.80 ± 0.50	31.3 ± 2.1	1.54 ± 0.12	19.5	4.44 ± 0.59	1.38 ± 0.19	0.17 ± 0.02	4.06 ± 0.34
JSH1-13	C-L3955	JSH1b-full	185–194	2.11 ± 0.12	32.5 ± 1.9	1.42 ± 0.02	19.1	5.82 ± 0.43	1.10 ± 0.18	0.16 ± 0.02	3.65 ± 0.31
JSH1-16	C-L3958	JSH1 OL	215–219	1.20 ± 0.30	17.0 ± 1.1	1.34 ± 0.18	24.9	6.55 ± 0.57	0.86 ± 0.11	0.16 ± 0.02	2.80 ± 0.26
JSH1-18	C-L3960	JSH1 OL	235–244	1.54 ± 0.29	19.7 ± 1.3	1.47 ± 0.11	18.9	5.96 ± 0.34	0.75 ± 0.13	0.15 ± 0.02	2.95 ± 0.27
JSH1-20	C-L3962	JSH1b-full	269–279	2.20 ± 0.40	20.7 ± 1.3	1.57 ± 0.12	19.1	6.09 ± 0.51	1.01 ± 0.14	0.15 ± 0.02	3.37 ± 0.29

Notes.
[a] Grain size for all samples was 100–200 μm.
[b] Measured water content values used in the calculation of dose rate, to which an uncertainty of ± 10% was applied.
[c] Internal K content was measured for each sample, but for dose rate calculations a value of 10 ± 2% was assumed, resulting in an internal beta dose of 0.502 ± 0.167 Gy/ka for all samples.
[d] Alpha efficiency value of 0.072 ± 0.003 used (see Supplementary Information for methods used to determine alpha-efficiency).
[e] A single dosimetry sample was measured for JSH1-6 and JSH1-7 due to their close proximity.

measurement conditions, prior to D_e determination using single-grains (section 5). Two different approaches were tested. First, an $IRSL_{50}$ SAR protocol (Wallinga et al., 2000) was investigated, because whilst the signal does not bleach as quickly as quartz, it does still bleach relatively quickly compared to many other feldspar signals obtained using higher stimulation temperatures (e.g. Buylaert et al., 2012; Colarossi et al., 2015). Secondly, a low-temperature post-IR IRSL protocol (Madsen et al., 2011; Reimann and Tsukamoto, 2012) was investigated. This protocol yields both an $IRSL_{50}$ signal, and a post-IR IRSL signal, which is likely to have a lower rate of anomalous fading than the $IRSL_{50}$ signal but a slower bleaching rate (e.g. Buylaert et al., 2012; Colarossi et al., 2015).

The impact of including a high-temperature clean-out step (Murray and Wintle, 2003) at the end of each post-IR IRSL measurement cycle (e.g. Thiel et al., 2011; Buylaert et al., 2012) was explored for the post-IR IRSL measurement procedure by stimulating with IR for 100 s while holding the sample at a temperature of 180 °C following each test dose measurement. Although this clean-out step is designed to remove any remaining signal at the end of each SAR cycle, it made no difference to our D_e or to our recuperation values measured from multiple-grain aliquots using both the $IRSL_{50}$ (pre-IR_{130}) and the post-IR $IRSL_{130}$ signal. For this reason, and to avoid the potential of introducing further sensitivity change, a high-temperature clean-out step was not included in the measurement sequences used to generate any of the data considered in this study.

The suitability of the $IRSL_{50}$ and post-IR IRSL protocols was tested with preheat, preheat dose-recovery (all dose-recovery data in this study is reported after subtracting the residual dose measured from grains that had been bleached for 24 h by the solar simulator), and residual dose preheat plateau tests, applied to sample JSH1-6.

4.1. Tests of the $IRSL_{50}$ protocol

The effect of preheat temperature was investigated for the first approach, the $IRSL_{50}$ protocol shown in Table 2a. Three aliquots were measured at each preheat temperature. Preheat temperatures ranged from 190 °C to 290 °C and were held for 10 s. For all measurements, the test dose signal (T_x) preheat conditions are the same as the preheat conditions of the natural and regenerative dose signal (L_x) (Blair et al., 2005).

Table 2
Measurement protocols used. MG = multiple grains, SG = single grains.

Step	Treatment	Observed
(a) $IRSL_{50}$ - MG		
1	Regenerative dose	
2	Preheat at 190 °C for 10 s	
3	IRSL Measurement (diodes) at 50 °C for 200 s	L_x
4	Test dose	
5	Preheat at 190 °C for 10 s	
6	IRSL Measurement (diodes) at 50 °C for 200 s	T_x
(b) Post-IR IRSL - MG		
1	Regenerative dose	
2	Preheat at 160 °C for 10 s	
3	IRSL Measurement (diodes) at 50 °C for 200 s	L_{x1}
4	IRSL Measurement (diodes) at 130 °C for 200 s	L_{x2}
5	Test dose	
6	Preheat at 160 °C for 10 s	
7	IRSL Measurement (diodes) at 50 °C for 200 s	T_{x1}
8	IRSL Measurement (diodes) at 130 °C for 200 s	T_{x2}
(c) Post-IR IRSL - SG		
1	Regenerative dose	
2	Preheat at 160 °C for 10 s	
3	IRSL Measurement (laser) at 50 °C for 2 s	L_{x1}
4	IRSL Measurement (laser) at 130 °C for 2 s	L_{x2}
5	Test dose	
6	Preheat at 160 °C for 10 s	
7	IRSL Measurement (laser) at 50 °C for 2 s	T_{x1}
8	IRSL Measurement (laser) at 130 °C for 2 s	T_{x2}

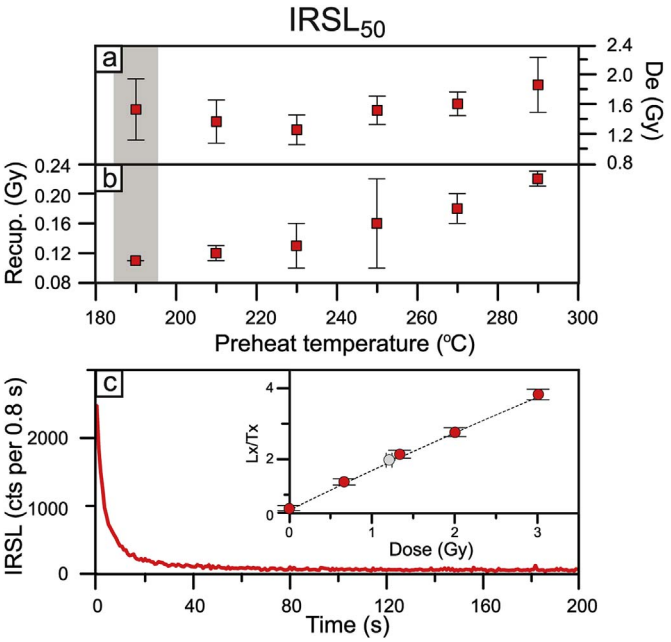

Fig. 3. Preheat plateau test results (values are arithmetic mean and standard deviation of three aliquots per temperature), signals and dose response curves for the $IRSL_{50}$ protocol (Table 2a).

The preheat plateau (Fig. 3a) shows no dependence of $IRSL_{50}$ D_e upon thermal pre-treatment, in accordance with the findings of Murray et al. (2009). Recuperation (expressed in Gy) increases with increasing preheat temperature (Fig. 3b), with the lowest value (0.11 ± 0.01 Gy, n = 3) being observed following a preheat at 190 °C. The lowest tested preheat temperature of 190 °C was chosen for further analyses in order to minimise recuperation and hence facilitate measurement of low natural doses. The suitability of this preheat temperature was validated with a dose-recovery test: six aliquots were bleached for 24 h in a Hönle SOL2 solar simulator, three of which were measured for dose-recovery (given dose: ~1.7 Gy) and the remaining three the residual dose.

A typical decay curve and dose-response curve for this $IRSL_{50}$ (preheat 190 °C) signal is shown in Fig. 3c. Data generated using this $IRSL_{50}$ (preheat 190 °C) protocol passed all performance tests (recycling ratio, test dose error, and dose-recovery test within 10% uncertainties), and the residual dose remaining after 24 h of bleaching in the Hönle SOL2 solar simulator was determined to be 0.20 ± 0.01 Gy (n = 3). The fading rate of the $IRSL_{50}$ (preheat 190 °C) signal was determined to be 2.9 ± 1.3%/decade for sample JSH1-6.

4.2. Tests of the post-IR IRSL protocol

For the second approach, tests on the suitability of different temperatures in the post-IR IRSL protocol (Table 2b) followed the same procedure as described in section 4.1 for the $IRSL_{50}$ signal. All post-IR IRSL measurements were preceded by an IRSL measurement at 50 °C, irrespective of preheat conditions. Preheat temperatures were tested in a range from 120 °C up to 240 °C, in steps of 20 °C, plus an additional temperature of 255 °C (selected so that the post-IR $IRSL_{225}$ signal that has been widely studied previously could be measured). All preheats were held for 10 s and were followed by post-IR IRSL measurements made at elevated temperatures that tracked the preheat temperature by −30 °C (termed the post-IR $IRSL_{elev}$ signal). The duration of the preheat

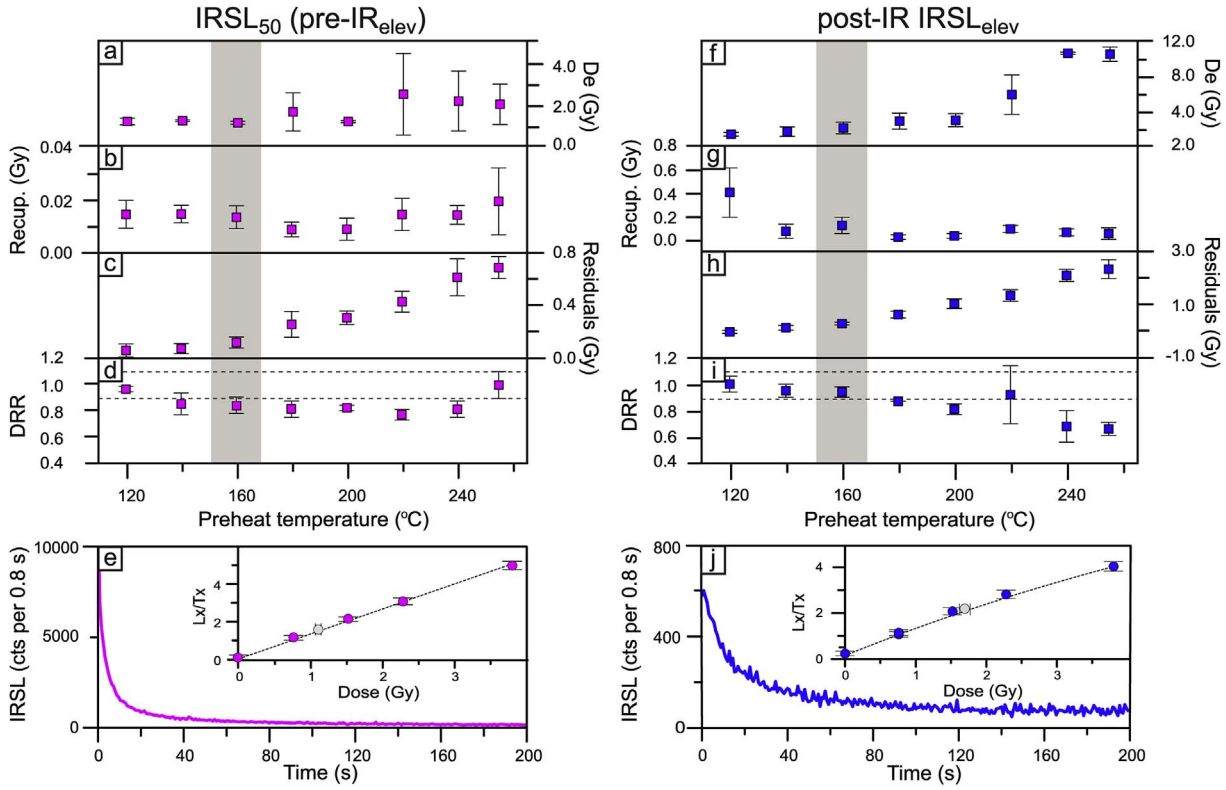

Fig. 4. Preheat plateau test results (values are arithmetic mean and standard deviation of three aliquots per temperature), including dose recovery ratios (DRR), residuals, signals and dose-response curves of feldspars. (a–e) for the $IRSL_{50}$ (pre-IR_{elev}) signal within a post-IR IRSL protocol; (f–j) for the post-IR $IRSL_{elev}$ signal within the same protocol. Decay curves and dose-response curves are shown for the highlighted preheat temperatures, which were also used for D_e determination.

was chosen based on the protocol proposed by Madsen et al. (2011) for young samples. We checked for any isothermal thermoluminescence contribution to our IRSL signals by measuring the signal with no optical stimulation for 5 channels before optical stimulation started. No isothermal signal was found. For all measurements, the natural or regenerative dose signal (L_x) and test dose signal (T_x) preheat conditions are the same as each other.

For each preheat temperature examined, six aliquots were bleached for 24 h in a Hönle SOL2 solar simulator. Three of these were used for a dose-recovery test (given dose: ~2.0 Gy) and the remaining three aliquots were used for measuring the residual dose.

4.2.1. $IRSL_{50}$ (pre-IR_{elev}) signal

The $IRSL_{50}$ (pre-IR_{elev}) signal shows no dependence of equivalent dose on preheat temperature (Fig. 4a), other than the size of the uncertainties on each equivalent dose determination typically increasing with increasing preheat temperature. The dose-recovery tests conducted at different temperatures suggest that the $IRSL_{50}$ (pre-IR_{elev}) signal can recover a dose within 1σ uncertainties for preheat temperatures of up to 160 °C (Fig. 4d). For preheat temperatures ≥180 °C (Fig. 4c), the residual dose measured following 24 h of bleaching in the SOL2 solar simulator increases with increasing preheat temperature. Taking the signal intensity, relative bleachability of signals (inferred from the residual dose values), recuperation and dose recovery test data into account (Fig. 4a–e), the $IRSL_{50}$ (pre-IR_{130}) protocol was identified as being suitable for further consideration in this study.

Is there any difference between data obtained using the $IRSL_{50}$ signal (protocol given in Table 2a) and the $IRSL_{50}$ (pre-IR_{130}) signal (protocol given in Table 2b) that might make one more suitable for dating than the other? Despite different preheat temperatures (i.e. 190 °C for the $IRSL_{50}$ protocol compared to 160 °C for the $IRSL_{50}$ (pre-IR_{130}) signal), the $IRSL_{50}$ luminescence signals measured within the post-IR $IRSL_{130}$ protocol are similar to the signals of the $IRSL_{50}$ protocol. Both signals are bright (1 mm aliquots yield several thousand counts per 0.8 s, e.g. Figs. 3c and 4e), and fading is identical within uncertainties (g_{2days} values of 2.92 ± 1.26 [n = 3, sample JSH1-6] and 3.24 ± 1.26%/decade [n = 3, JSH1-10] were measured for the $IRSL_{50}$ signal of two samples, and values for the $IRSL_{50}$ (pre-IR_{130}) signal varied between 1.84 ± 1.23%/decade [n = 3, JSH1-13] to 3.17 ± 1.26%/decade [n = 3, JSH1-10]). A mean of g_{2days} 2.48 ± 0.52%/decade was measured for the $IRSL_{50}$ (pre-IR_{130}) signal of all examined samples (n = 10). Measured residuals after 24 h of bleaching in a SOL2 are 0.20 ± 0.01 Gy and 0.12 ± 0.04 Gy, for the $IRSL_{50}$ and $IRSL_{50}$ (pre-IR_{130}) signal, respectively, both measured on sample JSH1-6. These results indicate further resetting of the signal when using the $IRSL_{50}$ (pre-IR_{130}). The recuperation of the $IRSL_{50}$ (pre-IR_{130}) signal (0.01 ± 0.00 Gy, n = 3, Fig. 4b) is lower than the recuperation of the $IRSL_{50}$ signal (0.11 ± 0.01 Gy, n = 3, Fig. 3b). In terms of age, this large difference in recuperation is equivalent to ~3 versus 30 years for the $IRSL_{50}$ (pre-IR_{130}) and $IRSL_{50}$ signals respectively, and could be significant for the samples in this study, where young, high-precision ages are required to test against the historical evidence for extreme wave events. Based on this evidence, the $IRSL_{50}$ (pre-IR_{130}) signal from the post-IR IRSL protocol (Table 2b) seems the most appropriate, but do the post-IR $IRSL_{elev}$ signals offer any advantage?

4.2.2. Post-IR $IRSL_{elev}$ signal

Over the range of preheat and post-IR IRSL stimulation temperatures tested, the post-IR IRSL signal intensity (Fig. 4j) is consistently an order of magnitude lower than either the $IRSL_{50}$ signal reported in section 4.1 (Fig. 3c), or the $IRSL_{50}$ (pre-IR_{elev}) signal measured as part of the post-IR IRSL protocol (section 4.2.1, Fig. 4e). Dose-recovery ratios (DRR) obtained using the post-IR $IRSL_{elev}$ signal are within 10% of unity (1σ uncertainty) for all preheat temperatures up to 220 °C (except for 200 °C; Fig. 4i). The residual dose remaining following 24 h of

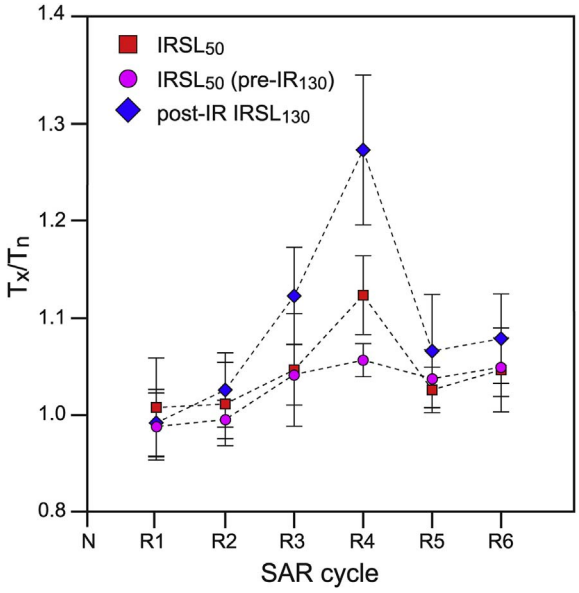

Fig. 5. Changes in response to the test dose during a SAR sequence for the $IRSL_{50}$ (Table 2a), $IRSL_{50}$ (pre-IR_{130}) and the post-IR $IRSL_{130}$ signals (Table 2b and c, respectively). The regenerative doses given in cycles 1 to 6 were 0.6, 1.2, 1.8, 2.6, 0.0 and 1.2 Gy respectively.

bleaching with the SOL2 solar simulator shows a steady increase with increasing temperature, rising from 0 Gy to 2.33 Gy for the post-IR $IRSL_{elev}$ signal (Fig. 4h).

The influence of charge carry-over on both signals, $IRSL_{50}$ (pre-IR_{130}) and post-IR $IRSL_{130}$, was observed by investigating changes in test dose sensitivity (Fig. 5). Larger variations in T_x/T_n of the post-IR $IRSL_{130}$ compared to the $IRSL_{50}$ (pre-IR_{130}) indicate a source of large recuperation in the post-IR $IRSL_{130}$ signal by carried-over charge, similar to that described by Colarossi et al. (in press) . Whilst this charge carry-over is significant for the post-IR $IRSL_{130}$, this second optical treatment (post-IR $IRSL_{elev}$) functions as an optical wash that removes any remaining charge from the $IRSL_{50}$ (pre-IR_{130}) signal. Particularly when dealing with very young samples, it is desirable to minimise thermal transfer in order to obtain more precise ages.

4.3. Selecting a protocol for equivalent dose determination

Based on the evidence described above, the post-IR $IRSL_{elev}$ signals are less appropriate for dating these young sediments than the $IRSL_{50}$ (pre-IR_{130}) signal, and so this latter signal was selected for equivalent dose determination. This decision is primarily based on the importance of minimising any residual signals or recuperation and was confirmed by measurements made on two samples collected from the current beach (JSH-MOD3 and JSH-MOD4).

Multiple-grain aliquot measurements yield unlogged central age model D_e values of 0.14 ± 0.00 Gy for JSH-MOD3 (wet beach sample) and 0.23 ± 0.04 Gy for JSH-MOD4 (dry beach sample) using the $IRSL_{50}$ (pre-IR_{130}) signal. In contrast much higher values are seen using the post-IR $IRSL_{130}$ signal (0.8 ± 0.02 Gy, wet beach sample; 1.28 ± 0.21 Gy, dry beach sample). These results are in agreement with the residual dose values measured following 24 h of bleaching within the Hönle SOL2 (for sample JSH1-6, Fig. 4c and h), and supports the decision to use the $IRSL_{50}$ (pre-IR_{130}) signal for dating.

5. Single-grain analysis

Samples from the current beach (JSH1-MOD3 and MOD4) give multiple grain D_e values that are not zero, even though they were thought to have been exposed to daylight during the years preceding collection. Additionally, the sediment samples in this study are believed to be derived from energetic tsunami or storm activity where exposure to daylight will be very limited during the final stage of erosion and deposition. Therefore, D_e determination using single-grains of feldspar was investigated so that heterogeneity of bleaching could be studied. The suitability of the measurement protocol was assessed by undertaking a dose recovery test, and single grain dose distributions were measured for all samples. Analysis of the shape of the D_e distributions was then undertaken in order to decide which age model should be used for age calculation.

5.1. Single grain dose recovery tests

Dose recovery experiments using single-grain measurements were undertaken on three samples (JSH1-4, −6 and −10). The post-IR $IRSL_{130}$ protocol described in Table 2c was used, and data for the $IRSL_{50}$ (pre-IR_{130}) signal used for analysis. Grains were bleached in the SOL2 solar simulator for 24 h prior to analysis. Two or three single grain discs had their D_e measured without any additional dose, and two or three discs received a known laboratory dose of 1.098 Gy. After screening, between 101 and 163 D_e values were obtained (Fig S-2). After subtraction of the dose measured in the grains that received no laboratory dose, the dose recovery ratios were 0.95 ± 0.02, 0.94 ± 0.02 and 0.96 ± 0.04, well within the standard acceptance criteria of 1.00 ± 0.10. This dose recovery experiment shows that the protocol used for these $IRSL_{50}$ (pre-IR_{130}) measurements (Table 2c) is effective at recovering a known laboratory dose. In all cases the dose recovery data were overdispersed (JSH1-4: 10.2 %; JSH1-6: 11.7 %; JSH1-10: 18.6 %), similar to the value of 16.5% overdispersion observed by Reimann et al. (2012) when measuring a sample that had received a known gamma dose.

5.2. Single grain D_e distributions

The same protocol used for the dose recovery test was then used for single grain measurements of the two samples collected from the current beach adjacent to the core site (Fig. 1b) and the ten samples collected from the two cores (Fig. 2). Examples of the dose distributions arising from these measurements are shown in Fig. 6, and data summarised in Table 3. All single grain equivalent dose distributions are provided in the supplementary material (Fig. S-3 and Fig. S-4).

For the natural signals measured, the D_e distributions are generally unimodal (e.g. Fig. 6a), but increase in width (e.g. Fig. 6b) with increasing depth down-core. In addition, for some of the samples, there are a small number of grains which give slightly larger D_e values compared to the overall distribution (e.g. Fig. 6c) and two samples (JSH1-2 and JSH1-20) where the range of D_e values is much greater (Fig. 6d) and where D_e values of many tens of Gray are found (e.g. JSH1-2 and JSH1-20; Fig. 6d). This may result from incomplete bleaching at deposition, but it is unclear whether this is also the explanation for the width of the distributions seen (e.g. Fig. 6b).

To explore the nature of the scatter in the single grain D_e data, Fig. 7 plots the overdispersion (OD) as a function of the D_e calculated with the unlogged central age model (CAM; Arnold et al., 2009, Fig. 7) for all 12 samples (Table 3). There is a linear relationship for all but two of the samples (JSH1-2 and JSH1-20, shown in red in Fig. 7); based on this trend these two samples have higher overdispersion than would be expected for their D_e, and are the samples, which exhibit a clear tail of grains with much higher D_e values (e.g. Fig. 6d). The unimodal nature of the other ten distributions and the linear increase in absolute overdispersion with age means that it is implausible that this overdispersion arises from incomplete bleaching at deposition. This explanation would require that each sample was systematically better-bleached at deposition than those laid-down by earlier events, and there is no reason to expect such a pattern.

The slope of the line in Fig. 7 is 0.45, implying that the relative

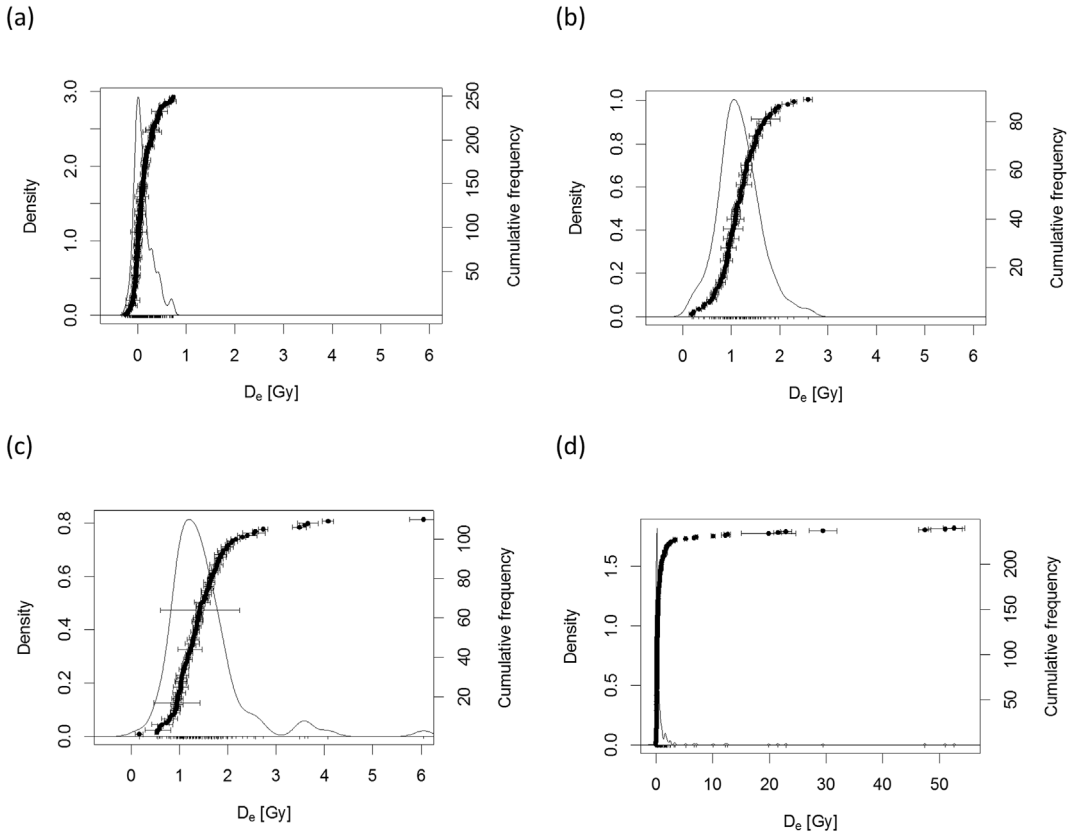

Fig. 6. Single grain dose distribution, shown as a Kernel Density Estimate (KDE) plot for (a) JSH-MOD3, (b) JSH1-9, (c) JSH1-6 and (d) JSH1-2. Note the different x-axis scale in (d).

overdispersion (OD) increases by 45 % of the D_e value. This is higher than the OD value of 20 % typically expected from well-bleached single grains of quartz (Arnold and Roberts, 2009), but there is little feldspar single grain data with which to compare these results. The single grain dose recovery experiments yielded overdispersion values between 10 and 19 %, and so OD values from samples irradiated in nature would be expected to be at least this magnitude. In addition to the sources of overdispersion that affect quartz, single grains of feldspar may have variable rates of anomalous fading, or different K concentrations leading to variable internal doses. Neudorf et al. (2012) observed high overdispersion (~38–47 %) in their single grain feldspar D_e values, a subset of which were corrected for grain-specific fading rates, but could not categorically demonstrate whether this resulted from post-depositional mixing or some other source. Smedley et al. (2016) working on glacial samples from the southern Andes suggested that samples that had overdispersion values of 50% or less had been well bleached. In light of these results, the slope of 0.45 in Fig. 7 is not unreasonable as the best estimate for the overdispersion characteristic of a well-bleached sample.

Fig. 7 shows that at least two of the samples have much higher OD than would be expected, and hence the minimum age model is applied in order to extract the most appropriate population for age calculation.

Table 3
Single grain equivalent dose data for the two samples from the modern beach and the 10 samples from the two cores. D_e values were obtained using the $IRSL_{50}$ (pre-IR_{130}) signal of the post-IR IRSL protocol (Table 2c). The number of D_e values (n) that passed acceptance criteria is shown, along with the unlogged CAM D_e, and the overdispersion calculated for the entire D_e data set for each sample.

Sample	n	CAM D_e (Gy)	CAM OD (Gy)	Calc. OD (Gy)[a]	Iterated OD (Gy)[b]	MAM D_e (Gy)	Proportion of D_e values included[c]
JSH-MOD3	249	0.11 ± 0.01	0.17	0.13	0.09	0.03 ± 0.01	0.64
JSH-MOD4	198	0.18 ± 0.02	0.23	0.16	0.13	0.12 ± 0.02	0.89
JSH1-2	240	1.14 ± 0.25	3.81	0.59	0.17	0.21 ± 0.02	0.84
JSH1-4	171	0.90 ± 0.04	0.52	0.48	0.45	0.82 ± 0.04	0.96
JSH1-6	110	1.47 ± 0.06	0.63	0.74	0.74	1.47 ± 0.18	1.00
JSH1-7	107	1.34 ± 0.07	0.65	0.68	0.67	1.30 ± 0.07	0.98
JSH1-9	90	1.16 ± 0.05	0.41	0.60	0.60	1.17 ± 0.10	1.00
JSH1-10	85	1.52 ± 0.10	0.88	0.77	0.68	1.37 ± 0.09	0.95
JSH1-13	114	1.59 ± 0.08	0.75	0.80	0.75	1.51 ± 0.08	0.97
JSH1-16	130	1.57 ± 0.07	0.70	0.79	0.76	1.50 ± 0.07	0.98
JSH1-18	111	2.01 ± 0.12	1.20	0.99	0.87	1.76 ± 0.09	0.94
JSH1-20	104	2.19 ± 0.27	2.70	1.07	0.86	1.74 ± 0.09	0.96

Notes.
[a] The calculated OD is the value derived for each sample from the relationship shown in Fig. 7.
[b] The iterated OD is the final value of OD obtained after applying the procedure described in section 5.3.
[c] The p0 parameter obtained from the minimum age model.

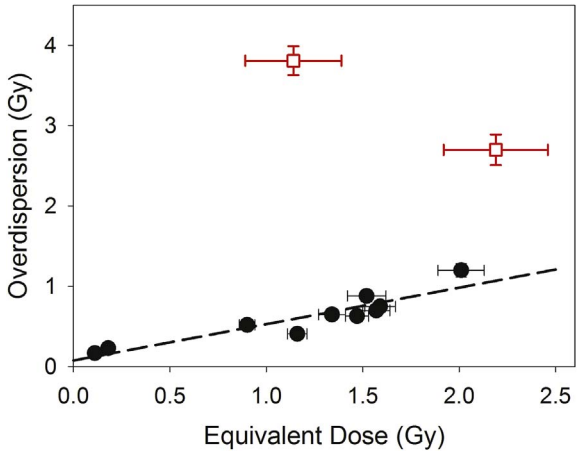

Fig. 7. Relationship between equivalent dose and the overdispersion (both calculated using the unlogged CAM) of the 12 single grain D_e data sets. The fitted line has a slope of 0.45 and an intercept of 0.08 Gy.

For consistency, the same age model was used for all samples. Where samples are well bleached the MAM will yield similar results to the CAM.

5.3. Application of the minimum age model

An unlogged 3-parameter minimum age model (MAM; Arnold et al., 2009) was applied to all samples, using overdispersion values derived from the relationship shown in Fig. 7. The unlogged MAM requires that sigma-b (the overdispersion of aliquots or single grains which have been well bleached at deposition) be specified as an absolute dose (in Gy), not as a percentage as required for the logged MAM (Galbraith et al., 1999). Since the absolute overdispersion of these samples seems to depend upon their D_e calculated for the sample (Fig. 7), an iterative approach was used. This involved calculating the OD value for each sample using the relationship shown in Fig. 7 and a D_e value calculated using the unlogged CAM. The OD value was then used as sigma-b to run the MAM model, yielding a new estimate of the D_e for the sample. This new estimate of D_e was then used to determine the OD from the relationship in Fig. 7, and this new value used to rerun the MAM. This iterative process rapidly converged (typically within 2 iterations) to stable values for the D_e and OD (Table 3). For most samples this process resulted in the inclusion of more than 95% of the D_e values (Table 3), excluding a small number of very high D_e values, and hence confirming that most samples were homogeneously bleached. For the two youngest samples (JSH-MOD3 and MOD4) a smaller proportion of grains was selected in this process, presumably because any incomplete bleaching at deposition will have a larger impact for younger samples.

The MAM D_e values are broadly similar to the CAM values (Table 3), with the exception of the two samples with much higher OD values (Fig. 7), and the samples from the current beach. In these cases the MAM yields smaller D_e values, as would be expected.

6. Results and discussion

6.1. Comparison with independent age control

Fig. 8 shows the fading-corrected $IRSL_{50}$ (pre-IR_{130}) ages determined for the 10 samples collected from two adjacent cores in the Shirasuka lowlands; the equivalent dose (D_e) values underpinning all of these $IRSL_{50}$ (pre-IR_{130}) ages were obtained using a single method of D_e distribution analysis, as outlined above (section 5). All data were corrected for anomalous fading using the average g_{2days}-value (2.48 ± 0.52%/decade) obtained previously (section 4.2.1). Buylaert et al. (2011) have shown that there is no improvement in precision by using aliquot-specific, or sample-specific fading rates. This approach is particularly appropriate in a geological setting where one would expect a similar provenance for all dated samples, as we interpret for the sediments in the cores studied here. The luminescence ages generated cover the age range from the 13th century CE until the mid 20th century CE (Table 4, Fig. 8) and are all in stratigraphic order. Although the central values for the ages of JSH1-6 and −7 (taken 15 cm apart in core JSH1/overlap, from within the same sand unit) are inverted, these samples are in agreement within the 1σ uncertainties shown, indicating rapid deposition and demonstrating the reproducibility of the luminescence analyses within this sand unit (Fig. 8).

The accuracy of the luminescence results can be assessed by comparing the ages with those obtained from radiocarbon dating of wood, and with aerial photography. The first comparison is provided by data from Garrett et al. (in press) who investigated cores taken adjacent to those used for luminescence dating in the present study. They obtained calibrated radiocarbon ages on wood from above (1282–1399 CE) and below (1040–1262 CE) the sedimentary unit of sample JSH1-20 in sediment core JSH1b/full. The $IRSL_{50}$ (pre-IR_{130}) age of 1390 CE (± 64 a) for JSH1-20 is consistent with these age estimates (Fig. 8).

A second comparison is for sample JSH1-2 at a depth of 47–53 cm, which is thought to be related to a landslide from the terrace immediately behind the coring site arising from an intense earthquake in 1944 CE. The landslide is recorded on aerial photography of the region in 1947 CE (Garrett et al., in press). The $IRSL_{50}$ (pre-IR_{130}) age of 1950 CE (± 8 a) would support this interpretation. It is interesting to note that this sample has an overdispersion that is higher than would be expected (Fig. 7); this too is consistent with its origin from landsliding. The agreement of the luminescence ages with independent age estimates, and the low residual doses seen in the two beach samples (0.03 ± 0.01 Gy for JSH-MOD3 and 0.12 ± 0.02 Gy for JSH–MOD4, Table 3) implies that when using the $IRSL_{50}$ (pre-IR_{130}) signal from single grains, residual signals and thermal transfer are not major impediments (cf. Li et al., 2017).

6.2. Integration with historical records and previous studies

The sedimentary record of the Shirasuka lowlands reveals a complex stratigraphy with laterally discontinuous sand sheets, reflecting deposition by extreme wave events. Radiocarbon dates published by Komatsubara et al. (2008) and Fujiwara et al. (2006) constrain the extreme wave event sedimentary record of the Shirasuka lowlands to be younger than 1200 CE. From 1200 CE onwards, at least six earthquakes and subsequent tsunamis occurred in segment C, D and E (Fig. 1a; Garrett et al., 2016). Additionally, large storm surges were reported to have inundated the lowlands several times (Komatsubara et al., 2008).

Lateral discontinuity between the sand layers recorded in cores taken from this site has previously been described by Komatsubara et al. (2008), and this lateral discontinuity is also noted in this study for cores JSH1b/full and JSH1/overlap even though they are only 0.5 m apart (Fig. 2). However, correlation between the two cores in the present study, and potential links to the record of Komatsubara et al. (2008), can be aided by the luminescence ages generated (Fig. 8). The lowermost sand unit in JSH1b/full (Figs. 2 and 8) is radiocarbon dated to 1040–1262 CE and is identified as the former beach (Garrett et al., in press). A minimum age for sand unit 4 in JSH1b/full is given by the radiocarbon age (1282–1399 CE; sampled in sediment core JSH1b/full, see Fig. 8) of plant macrofossils (Garrett et al. in press), and $IRSL_{50}$ (pre-IR_{130}) ages of 1291 CE ± 78 a (sample JSH1-18, core JSH1/overlap), 1364 CE ± 72 a (sample JSH1-16, core JSH1-/overlap) and 1390 CE ± 64 a (sample JSH1-20; core JSH1-b/full) overlap within 1-2σ uncertainties. Sand 4 (Figs. 2 and 8) in each core can be correlated on the basis of age with unit A of Komatsubara et al. (2008), which they date to 1270–1360 CE using radiocarbon dating, and which they interpret to be derived from terrace material based upon the mica content. The luminescence ages for sand unit 4 containing JSH1-18, JSH1-

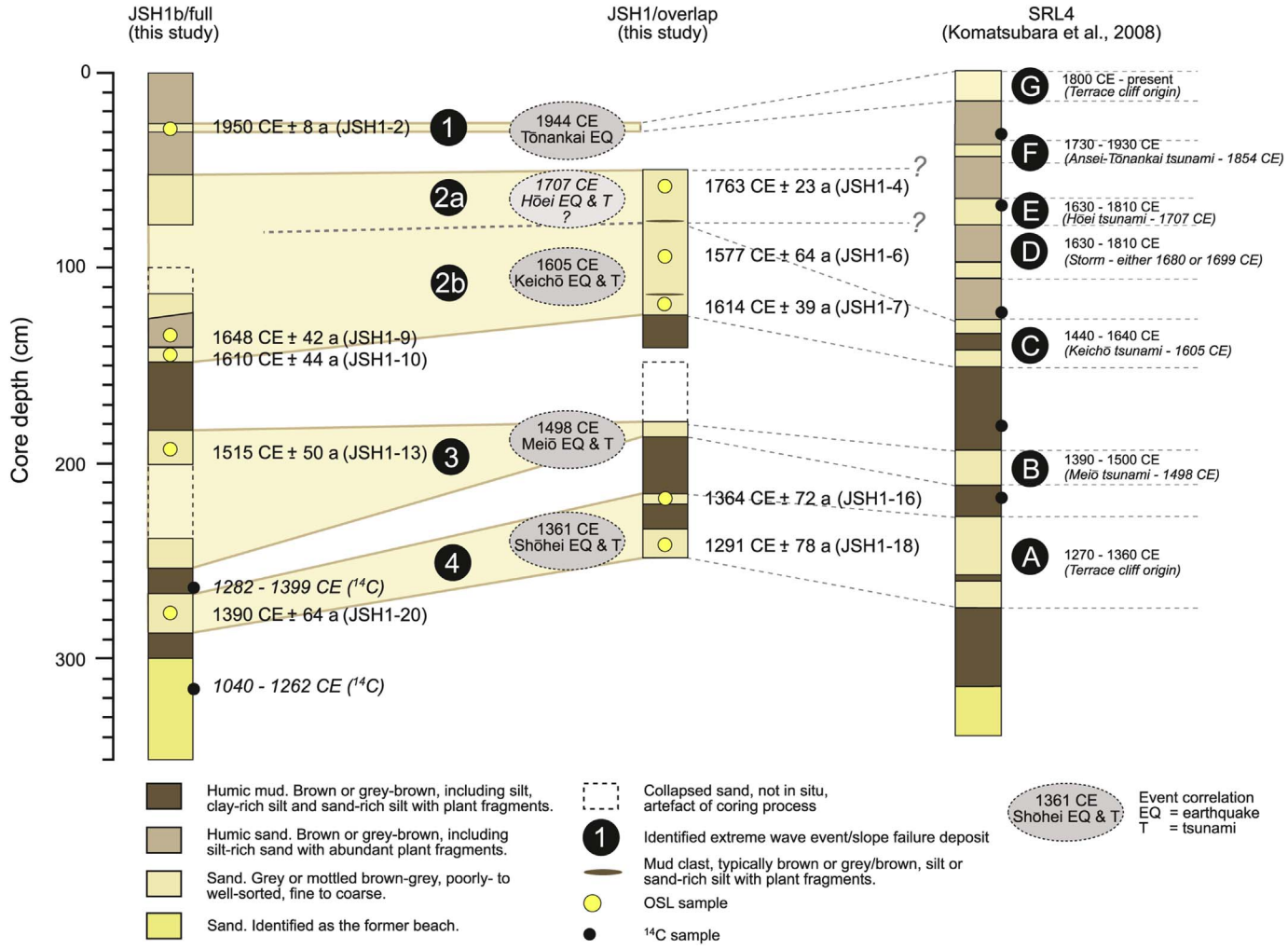

Fig. 8. Stratigraphy and chronology based on $IRSL_{50}$ (pre-IR_{130}) ages for the Shirasuka lowlands, in comparison to previous results by Komatsubara et al. (2008). Sand layers 1, 2, 3 and 4 identified in Fig. 2 are shown. Based on the IRSL ages, unit 2 is thought to represent two closely spaced events (2a and 2b). Letters A to G are sands related to events identified by Komatsubara et al. (2008). The presented radiocarbon ages are published in Garrett et al. (in press) .

Table 4
Fading rates, D_e values, dose rates and ages for the 10 samples from the cores. D_e values were obtained using the $IRSL_{50}$ (pre-IR_{130}) signal of the post-IR IRSL protocol (Table 2c).

Sample	Fading ($g_2$days, %/decade)	MAM D_e (Gy)	Dose Rate (Gy/ka)	Fading corrected age (a)[a]	Date (CE)[b]
JSH1-2	2.72 ± 1.24	0.21 ± 0.02	3.83 ± 0.31	65 ± 8	1950 ± 8
JSH1-4	2.52 ± 1.24	0.82 ± 0.04	3.92 ± 0.27	252 ± 23	1763 ± 23
JSH1-6	3.09 ± 1.31	1.47 ± 0.18	4.06 ± 0.33	438 ± 64	1577 ± 64
JSH1-7	2.07 ± 1.27	1.30 ± 0.07	3.91 ± 0.30	401 ± 39	1614 ± 39
JSH1-9	2.84 ± 1.25	1.17 ± 0.10	3.82 ± 0.26	367 ± 42	1648 ± 42
JSH1-10	3.17 ± 1.26	1.37 ± 0.09	4.06 ± 0.34	405 ± 44	1610 ± 44
JSH1-13	1.84 ± 1.23	1.51 ± 0.08	3.65 ± 0.31	500 ± 50	1515 ± 50
JSH1-16	1.91 ± 1.24	1.50 ± 0.07	2.80 ± 0.26	651 ± 72	1364 ± 72
JSH1-18	1.86 ± 1.23	1.76 ± 0.09	2.95 ± 0.27	724 ± 78	1291 ± 78
JSH1-20	2.76 ± 1.25	1.74 ± 0.09	3.37 ± 0.29	625 ± 64	1390 ± 64

Notes.
[a] Ages have been fading corrected using the average fading rate of 2.48 ± 0.52%/decade.
[b] Dates have been calculated using a datum of 2015 CE when the samples were collected.

16 and −20 (1291 CE ± 78 a, 1364 CE ± 72 a and 1390 CE ± 64 a) are consistent with the Kōan (also known as Shōhei) earthquake and tsunami, which occurred in 1361 CE. Based on the historical documents, this earthquake has so far been interpreted as a rupture of the western segements of the Nankai trough (segment A and B). Ishibashi (2004) mentioned the possibility of a synchronous rupture of the eastern and western segments of the Nankai Trough in 1361 CE, or even the possibility of a separate rupture of the eastern segments two days prior to the earthquake of the segments A and B (Ishibashi and Satake, 1998; Ishibashi, 2014). No tsunami deposits in the eastern Nankai region have been reported from this event, but this sand sheet could give the first evidence for tsunami inundation in this region.

Sand 3 (Figs. 2 and 8) has little chronological control from this study, making correlation between cores on the basis of chronology impracticable. However, sample JSH1-13 from core JSH1/full yields a date of 1515 CE (± 50 a), which correlates well with the Meiō tsunami of 1498 CE (Komatsubara et al.'s unit B). Komatsubara et al. (2008) also correlated their Unit B with the Meiō tsunami on the basis of radiocarbon dating of their core (Fig. 8; 1390–1500 CE; Komatsubara et al., 2008), taken ~20 m away from the cores in this study. Inundation of the Enshu-nada coastline by the Meiō tsunami has already been demonstrated (e.g. Fujiwara et al., 2013), making it a reasonable assumption to find some evidence of this event preserved in the Shirasuka lowlands stratigraphy.

Continuing upward through the sequences of the two cores, the next dated sand unit (sand 2) in each case contains samples JSH1-10 (from core JSH1/full) and JSH1-6 and −7 (from core JSH1/overlap). The three luminescence ages obtained (1610 CE (± 44 a), 1577 CE (± 64 a) and 1614 CE (± 39 a), respectively) are tightly clustered, and can be

correlated with unit C of Komatsubara et al. (2008), which they associated with the 1605 CE Keichō tsunami. The three luminescence ages provide a much more precise association with this event than the radiocarbon ages of Komatsubara et al. (2008) which gave a wide envelope for the age of their Unit C ranging from 1440 to 1640 AD. Sample JSH1-9 comes from the finer deposit that caps this sand unit in core JSH1/full, but was later interpreted to be a rip-up clast. The date of 1648 CE (± 42 a) is also consistent with the underlying sand originating from the 1605 CE tsunami. The age of JSH1-9, and the presence of this fine unit between two sand units in core JSH1-full, also implies that the overlying sand units probably relate to a different event. Indeed, the date of 1763 CE (± 23 a) for JSH1-4, taken from the uppermost part of sand unit 2, is statistically distinct from the ages obtained for the lower part of sand unit 2 (which contains JSH-6 and -7), suggesting that unit 2 records two discrete events (labelled 2a and 2b on Fig. 8). It is not immediately obvious what historical event unit 2a correlates with, or which unit of Komatsubara et al. (2008) it might correspond to (i.e. Unit D, E or F), if any. The extreme wave event closest in time is the 1707 CE Hōei tsunami, although the luminescence age is ~2.5 standard deviations from this event. Interestingly, the 1751 CE Concepción (Chile) tsunami also lies within the age range from luminescence dating (1763 CE ± 23 a), and is known to have crossed the Pacific and inundated parts of the Japanese coastline (e.g. Sendai and Wakayama; Atwater et al., 2015); however, there is no historical evidence for inundation along the Enshu-nada coast at this time (Watanabe, 1998).

As discussed previously, JSH1-2, the uppermost sand unit in core JSH1/full, gave a luminescence age of 1950 CE (± 8 a) and this correlates well with the 1944 CE Tōnankai earthquake that affected this region. Although this 1944 CE earthquake caused a tsunami, its wave height (~0.9 m) was too small to overwash the coastal dune. Komatsubara et al. (2008) used radiocarbon dating to constrain their Unit G with which this correlates, describing it as being derived from terrace material, but a radiocarbon plateau at this time meant that the age constraints were very limited (younger than 1800–1930 CE). The luminescence age in the present study (Table 3, Fig. 8) provides a much tighter constraint on the timing of emplacement of this sand unit.

7. Summary and conclusions

This study tested the suitability of luminescence dating to constrain the age of young (< 1000 years) extreme wave event deposits from the Shirasuka lowlands, Japan. Unsurprisingly, and in accordance with other studies, quartz was found to be unsuitable for dating. Coarse grains of alkali-feldspar were tested and subsequently used for dating. The $IRSL_{50}$ signal measured as part of a post-IR_{50} $IRSL_{130}$ protocol was found to be most suitable for dating these deposits.

The degree of bleaching of the Shirasuka sediment samples taken for luminescence dating was assessed by examining single coarse-grains of alkali-feldpsars. The $IRSL_{50}$ (pre-IR_{130}) single grain distributions were surprisingly well-bleached, given the expectation that these were taken from extreme wave event deposits. Nevertheless, each sample contained a small proportion of grains with larger-than-expected D_e values, and for each sample the overdispersion values typically scaled with the D_e value. The unlogged minimum age model was therefore applied to the D_e data from these young sediments, using a novel iterative method for estimating the absolute overdispersion value (in Gy). This approach enabled a single method of D_e distribution analysis to be applied to all samples in this study, and resulted in fading-corrected $IRSL_{50}$ (pre-IR_{130}) ages which that were both internally consistent, and that could also be correlated to other evidence for extreme wave events in this region, including the historical record and independent dating evidence.

The fading-corrected $IRSL_{50}$ (pre-IR_{130}) ages demonstrate that the two cores in this study span the historical record of extreme wave event deposits in this region. The luminescence ages also demonstrate that it is possible to differentiate between individual events that occurred within the past 800 years. These $IRSL_{50}$ (pre-IR_{130}) ages can be linked to the presence and impact of tsunamis in 1361 CE, 1498 CE, and 1605 CE, and also to a slope failure driven by the 1944 CE Tōnankai earthquake. The absence of sand layers driven by other major known extreme wave events in this region, such as the 1707 CE Hōei tsunami and the 1854 CE Ansei-Tōnankai earthquake and tsunami events, is potentially due to issues of preservation such as lateral discontinuity of the sand sheets.

In some cases, the luminescence dates generated in this study constrain the extreme wave event units more precisely than the radiocarbon dating, due to plateau within the ^{14}C-calibration curve around the time of interest. This study highlights the great potential for using luminescence dating, including using a signal from feldspars, to date even young extreme wave event deposits in both this region, and potentially elsewhere.

Acknowledgements

This research was undertaken as part of the QuakeRecNankai project, funded by the Belgian Science Policy Office (BELSPO BRAIN-be BR/121/A2). SR's MSc studies were financially supported by the Deutschlandstipendium scholarship, which is gratefully acknowledged. A research stay of SR at the Aberystwyth Luminescence Research Laboratory (ALRL), Aberystwyth University (UK) was possible due to a DAAD (German Academic Exchange Service) PROMOS student mobility scholarship. SR would like to thank the Arbeitskreis für Geomorphologie (German Working group of Geomorphologists) for financially supporting her participation in the UK Luminescence and ESR meeting 2016, where this work was presented. GEK acknowledges financial support from Swiss National Science Foundation grant PZ00P2_167960. Hollie Wynne (Aberystwyth University, UK) is thanked for her help in the ALRL. Hanna Cieszynski (University of Cologne, Germany) took the REM images. Ian Bailiff (Durham University, UK) is thanked for providing the spreadsheet, which was used to correct for layer-to-layer variations in gamma dose rate according to Aitken (1985). All authors would like to acknowledge the support by local authorities and the landowners, who permitted fieldwork in the paddy fields We would like to thank Dr. Sumiko Tsukamoto and an anonymous referee for their comments, which helped to improve this paper.

This is a contribution to IGCP project 639 “Sea-level changes from minutes to millennia” and INQUA Project CMP1701P.

Appendix A. Supplementary data

Supplementary data related to this article can be found at http://dx.doi.org/10.1016/j.quageo.2018.01.006.

References

Adamiec, G., Aitken, M.J., 1998. Dose-rate conversion factors: update. Anc. TL 16, 37–50.
Aitken, M.J., 1985. Thermoluminescence Dating. Academic Press, London 359pp.
Ando, M., 1975. Source mechanisms and tectonic significance of historical earthquakes along the Nankai trough. Jpn. Tectonophys. 27, 119–140.
Arnold, L.J., Roberts, R.G., 2009. Stochastic modelling of multi-grain equivalent dose (*De*) distributions: implications for OSL dating of sediment mixtures. Quat. Geochronol. 4, 204–230.
Arnold, L.J., Roberts, R.G., Galbraith, R.F., DeLong, S.B., 2009. A revised burial dose estimation procedure for optical dating of young and modern-age sediments. Quat. Geochronol. 4, 306–325.
Atwater, B.F., Satoko, M.-R., Kenji, S., Yoshinobu, T., Kazue, U., Yamaguchi, D.K., 2015. The Orphan Tsunami of 1700 – Japanese Clues to a Parent Earthquake in North America. University of Washington Press, Washington 135 pp.
Auclair, M., Lamothe, M., Huot, S., 2003. Measurement of anomalous fading for feldspar IRSL using SAR. Radiat. Meas. 37, 487–492.
Bell, W.T., 1980. Alpha attenuation in quartz grains for thermoluminescence dating. Anc. TL 12, 4–8.
Bishop, P., Sanderson, D., Hansom, J., Chaimanee, N., 2005. Age- dating of tsunami deposits: lessons from the 26 December 2004 tsunami in Thailand. Geogr. J. 171,

379–384.
Blair, M., Yukihara, E.G., McKeever, S.W.S., 2005. Experiences with single-aliquot OSL procedures using coarse-grain feldspars. Radiat. Meas. 39, 361–374.
Brill, D., Klasen, N., Jankaew, K., Bru¨ckner, H., Kelletat, D., Scheffers, A., Scheffers, S., 2012a. Local inundation distances and regional tsunami recurrence in the Indian Ocean inferred from luminescence dating of sandy deposits in Thailand. Nat. Hazards Earth Syst. Sci. 12, 2177–2192.
Brill, D., Klasen, N., Brückner, H., Jankaew, K., Scheffers, A., Kelletat, D., Scheffers, S., 2012b. OSL dating of tsunami deposits from Phra Thong Island. Thailand. Quat. Geochronol. 10, 224–229.
Brill, D., May, M.S., Engel, M., Reyes, M., Pint, A., Opitz, S., Dierick, M., Gonzalo, L.A., Esser, S., Brückner, H., 2016. Typhoon Haiyan's sedimentary record in coastal environments of the Philippines and its palaeotempestological implications. Nat. Hazards Earth Syst. Sci. 16 7299–2822.
Buylaert, J.-P., Huot, S., Murray, A.S., van den Haute, P., 2011. Infrared stimulated luminescence dating of an Eemian (MIS 5e) site in Denmark using K-feldspar. Boreas 40, 46–56.
Buylaert, J.-P., Murray, A.S., Thomsen, K.J., Thiel, C., Sohbati, R., 2012. A robust feldspar luminescence dating method for Middle and Late Pleistocene sediments. Boreas 41, 435–451.
Chagué-Goff, C., Schneider, J.-L., Goff, J.R., Dominey-Howes, D., Strotz, L., 2011. Expanding the proxy toolkit to help identify past events – lessons from the 2004 Indian Ocean tsunami and the 2009 South Pacific tsunami. Earth Sci. Rev. 107, 107–122.
Colarossi, D., Duller, G.A.T., Roberts, H.M., Tooth, S., Lyons, R., 2015. Comparison of paired quartz OSL and feldspar post-IR IRSL dose distributions in poorly bleached fluvial sediments from South Africa. Quat. Geochronol. 30, 233–238.
Colarossi, D., Duller, G.A.T. and Roberts, H.M., Exploring the behaviour of luminescence signals from feldspars: implications for the single aliquot regenerative dose protocol. Radiat. Meas., in press. https://doi.org/10.1016/j.radmeas.2017.07.005.
Cunha, P.P., Buylaert, J.P., Murray, A.S., Andrade, C., Freitas, M.C., Fatela, F., Munhá, J.M., Martins, A.A., Sugisaki, S., 2010. Optical dating of clastic deposits generated by an extreme marine coastal flood: the 1755 tsunami deposit in the Algarve (Portugal). Quat. Geochronol. 5, 329–335.
Cunningham, A.C., Bakker, M.A.J., van Heteren, S., van der Valk, B., van der Spek, A.J.F., Schaart, D.R., Wallinga, J., 2011. Extracting storm-surge data from coastal dunes for improved assessment of flood risk. Geology 39 (11), 1063–1066.
Dawson, A.G., Stewart, I., 2007. Tsunami deposits in the geological record. Sediment. Geol. 200, 166–183.
Durcan, J.A., King, G.E., Duller, G.A.T., 2015. DRAC: dose rate and age calculator for trapped charge dating. Quat. Geochronol. 28, 54–61.
Engel, M., Brückner, H., Wennrich, V., Scheffers, A., Kelletat, D., Vött, A., Schäbitz, F., Daut, G., Willershäuser, T., May, S.M., 2010. Coastal stratigraphies of eastern Bonaire (Netherlands Antilles): new insights into the palaeo-tsunami history of the southern Caribbean. Sediment. Geol. 231, 14–30.
Fujiwara, O., Komatsubara, J., Takada, K., Shishikura, M., Kamataki, T., 2006. Temporal development of a late Holocene strand plain system in the Shirasuka area along western Shizuoka Prefecture on the Pacific coast of central Japan. Chigaku Zasshi 115, 569–581 (In Japanese).
Fujiwara, O., Ono, E., Yata, T., Umitsu, M., Sato, Y., Heyvaert, V.M.A., 2013. Assessing the impact of 1498 Meio earthquake and tsunami along the Enschu-nada coast, central Japan using coastal geology. Quat. Int. 308–309, 4–12.
Galbraith, R.F., Roberts, R.G., Laslett, G.M., Yoshida, H., Olley, J.M., 1999. Optical dating of single and multiple grains of quartz from Jinmium Rock Shelter, Northern Australia: Part I, experimental design and statistical models. Archaeometry 41 (2), 339–364.
Garrett, E., Fujiwara, O., Garrett, P., Heyvaert, V.M.A., Shishikura, M., Yokoyama, Y., Hubert-Ferrari, A., Brückner, H., Nakamura, A., De Batist, M., the QuakeRecNankai team, 2016. A systematic review of geological evidence for Holocene earthquakes and tsunamis along the Nankai-Suruga Trough, Japan. Earth Sci. Rev. 159, 337–357.
Garrett, E., Fujiwara, O., Riedesel, S., Walstra, J., Deforce, K., Yokoyama, Y., Schmidt, S., Brückner, H., De Batist, M., Heyvaert, V.M.A., QuakeRecNankai team, in press. Historical Nankai-Suruga megathrust earthquakes recorded by tsunami and terrestrial mass movement deposits on the Shirasuka coastal lowlands, Shizuoka Prefecture, Japan. Holocene. DOI: 10.1177/0959683617752844.
Goff, J., Ebina, Y., Goto, K., Terry, J., 2016. Defining tsunamis: yoda strikes back? Earth Sci. Rev. 159, 271–274.
Guérin, G., Mercier, N., Nathan, R., Adamiec, G., Lefrais, Y., 2012. On the use of the infinite matrix assumption and associated concepts: a critical review. Radiat. Meas. 47, 778–785.
Huntley, D.J., Clague, J.J., 1996. Optical dating of tsunami-laid sands. Quat. Res. 46, 127–140.
Huntley, D.J., Lamothe, M., 2001. Ubiquity of anomalous fading in K-feldspars and the measurement and correction for it in optical dating. Can. J. Earth Sci. 38, 1093–1106.
Ishibashi, K., 2014. Nankai Trough Great Earthquake – History, Science and Society. Iwanami Shoten, Tokyo 205pp.
Ishibashi, K., 2004. Status of historical seismology in Japan. Ann. Geophys. 47 (2/3), 339–368.
Ishibashi, K., Satake, K., 1998. Problems on forecasting great earthquakes in the subduction zones around Japan by means of paleoseismology. Zisin 50, 1–21.
Jankaew, K., Atwater, B.F., Sawai, Y., Choowong, M., Charoentitirat, T., Martin, M.E., Prendergast, A., 2008. Medieval forewarning of the 2004 Indian Ocean tsunami in Thailand. Nature 455, 1228–1231.
Kars, R.H., Reimann, T., Ankjaergaard, C., Wallinga, J., 2014. Bleaching of the post-IR IRSL signal: new insights for feldspar luminescence dating. Boreas 43, 780–791.
Komatsubara, J., Fujiwara, O., Takada, K., Sawai, Y., Aung, T.T., Kamataki, K., 2008. Historical tsunamis and storms recorded in a coastal lowland, Shizuoka Prefecture, along the Pacific coast of Japan. Sedimentology 55, 1703–1716.
Kondo, R., Tsukamoto, S., Tachibana, H., Miyairi, Y., Yokoyama, Y., 2007. Age of glacial and periglacial landforms in northern Hokkaido, Japan, using OSL dating of fine grain quartz. Quat. Geochronol. 2, 260–265.
Kreutzer, S., 2016. calc_FadingCorr(): apply a fading correction according to Huntley & Lamothe (2001) for a given g-value and a given tc. Function version 0.4.2. In: Kreutzer, S., Dietze, M., Burow, C., Fuchs, M.C., Schmidt, C., Fischer, M., Friedrich, J. (Eds.), Luminescence: Comprehensive Luminescence Dating Data Analysis, R package version 0.6.4. https://CRAN.R-project.org/package=Luminescence.
Kreutzer, S., Schmidt, C., Fuchs, M.C., Dietze, M., Fischer, M., Fuchs, M., 2012. Introducing an R package for luminescence dating analysis. Ancient TL 30 (1), 1–8.
Li, Y., Tsukamoto, S., Hu, K., Frechen, M., 2017. Quartz OSL and K-feldspar post-IR IRSL dating of sand accumulation in the lower Liao Plain (Liaoning, NE China). Geochronometria 44, 1–15.
Loveless, J.P., Meade, B.J., 2010. Geodetic imaging of plate motions, slip rates, and partitioning of deformation in Japan. J. Geophys. Res. 115, B02410.
Madsen, A.,T., Buylaert, J.-P., Murray, A.S., 2011. Luminescence dating of young coastal deposits from New Zealand using feldspars. Geochronometria 38 (4), 378–390.
Madsen, A.T., Duller, G.A.T., Donnelly, J.P., Roberts, H.M., Wintle, A.G., 2009. A chronology of hurricane landfalls at Little Sippewissett Marsh, Massachusetts, USA, using optical dating. Geomorphology 109, 36–45.
Madsen, A.T., Murray, A.S., 2009. Optically stimulated luminescence dating of young sediments: a review. Geomorphology 109, 3–16.
May, S.M., Falvard, S., Norpoth, M., Pint, A., Brill, D., Engel, M., Scheffers, A., Dierick, M., Paris, R., Squire, P., Brückner, H., 2016. A mid-Holocene candidate tsunami deposit from the NW Cape (Western Australia). Sediment. Geol. 332, 40–50.
Mazzotti, S., Le Pichon, X., Henry, P., Miyazaki, S., 2000. Full interseismic locking of the Nankai and Japan-west Kurile subduction zones: an analysis of uniform elastic strain accumulation in Japan constrained by permanent GPS. J. Geophys. Res. Solid Earth 105, 13159–13177.
Monecke, K., Finger, W., Klarer, D., Kongko, W., McAdoo, B.G., Moore, A.L., Sudrajat, S.U., 2008. A 1,000-year sediment record of tsunami recurrence in northern Sumatra. Nature 455 (30), 1232–1234.
Morton, R.A., Gelfenbaum, G., Jaffe, B.E., 2007. Physical criteria for distinguishing sandy tsunami and storm deposits using modern examples. Sediment. Geol. 200, 184–207.
Murari, M.K., Achyuthan, H., Singhvi, A.K., 2007. Luminescence studies on the sediments laid down by the December 2004 tsunami event: Prospects for the dating of palaeo tsunamis and for the estimation of sediment fluxes. Science 92 (3), 367–371.
Murray, A.S., Wintle, A.G., 2003. The single aliquot regenerative dose protocol: potential for improvements in reliability. Radiat. Meas. 37, 377–381.
Murray, A.S., Buylaert, J.P., Thomsen, K.J., Jain, M., 2009. The effect of preheating on the IRSL signal from feldspar. Radiat. Meas. 44, 554–559.
Neudorf, C.M., Lian, O.B., Walker, I.J., Shugar, D.H., Eamer, J.B.R., Griffin, L.C.M., 2015. Toward a luminescence chronology for coastal dune and beach deposits on Calvert Island, British Columbia central coast, Canada. Quat. Geochronol. 30, 275–281.
Neudorf, C.M., Roberts, R.G., Jacobs, Z., 2012. Sources of overdispersion in a K-rich feldspar sample from north-central India: insights from D_e, K content and IRSL age distributions for individual grains. Radiat. Meas. 47, 696–702.
Pilarczyk, J.E., Horton, B.P., Soria, J.L.A., Switzer, A.D., Siringan, F., Fritz, H.M., Khan, N.S., Ildefonso, S., Doctor, A.A., Garcia, M.I., 2016. Micropaleontology of the 2013 Typhoon Haiyan overwash sediments from the leyte Gulf, Philippines. Sediment. Geol. 339, 104–114.
Prendergast, A.L., Cupper, M.L., Jankaew, K., Sawai, Y., 2012. Indian Ocean tsunami recurrence from optical dating of tsunami sand sheets in Thailand. Mar. Geol. 295–298, 20–27.
Prescott, J.R., Hutton, J.T., 1994. Cosmic ray contributions to dose rates for lumi- nescence and ESR dating: large depths and long-term time variations. Radiat. Meas. 23, 497–500.
Reimann, T., Tsukamoto, S., 2012. Dating the recent past (< 500) by post-IR IRSL feldspar – examples from the North Sea and Baltic Sea coast. Quat. Geochronol. 10, 180–187.
Reimann, T., Thomsen, K.J., Jain, M., Murray, A.S., Frechen, M., 2012. Single-grain dating of young sediments using the pIRIR signal from feldspar. Quat. Geochronol. 11, 28–41.
Satake, K., 2015. Geological and historical evidence of irregular recurrent earthquakes in Japan. Phil. Trans. R. Soc. A 373, 1–10.
Shanmugam, G., 2012. Process-sedimentological challenges in distinguishing paleo-tsunami deposits. Nat. Hazards 63, 5–30.
Smedley, R.K., Glasser, N.F., Duller, G.A.T., 2016. Luminescence dating of glacial advances at Lago Buenos Aires (~46 °S), Patagonia. Quat. Sci. Rev. 134, 59–73.
Smedley, R.K., Duller, G.A.T., Pearce, N.J.G., Roberts, H.M., 2012. Determining the K-content of single-grains of feldspar for luminescence dating. Radiat. Meas. 47, 790–796.
Soria, J.L.A., Switzer, A.D., Pilarczyk, J.E., Siringan, F.P., Khan, N.S., Fritz, H.M., 2017. Typhoon Haiyan overwash sediments from Leyte Gulf coastlines show local spatial variations with hybrid storm and tsunami signatures. Sediment. Geol. 358, 121–138.
Spiske, M., Piepenbreier, J., Benavente, C., Kunz, A., Bahlburg, H., Steffahn, J., 2013. Historical tsunami deposits in Peru: Sedimentology, inverse modelling and optically stimulated luminescence dating. Quat. Int. 305, 31–44.
Steffen, D., Preusser, F., Schlunegger, F., 2009. OSL quartz age underestimation due to unstable signal components. Quat. Geochronol. 4, 353–362.
Stuiver, M., 1978. Radiocarbon timescale tested against magnetic and other dating methods. Nature 273, 271–274.
Switzer, A.D., Srinivasalu, S., Thangadurai, N., Ram Mohan, V., 2012. Bedding structures in Indian tsunami deposits provide clues to the dynamics of tsunami inundation. In:

In: Terry, J., Goff, J. (Eds.), Natural Hazards in the Asia – Pacific Region: Recent Advantages and Emerging Concepts, vol. 361. Geol. Soc. London Spec. Pub., London, pp. 61–77.
Tamura, T., Sawai, Y., Ito, K., 2015. OSL dating of the AD 869 Jogan tsunami deposit, northeastern Japan. Quat. Geochronol. 30, 294–298.
Thiel, C., Buylaert, J.-P., Murray, A., Terhorst, B., Hofer, I., Tsukamoto, S., Frechen, M., 2011. Luminescence dating of the Stratzing loess profile (Austria) – testing the potential of an elevated temperature post-IR IRSL protocol. Quat. Int. 234, 23–31.
Tsukamoto, S., Rink, W.J., Watanuki, T., 2003. OSL of tephric loess and volcanic quartz in Japan and an alternative procedure for estimating De from a fast OSL component. Radiat. Meas. 37, 459–465.
Usami, T., 1979. Study of historical earthquakes in Japan. Bull. Earthq. Res. Inst. 54, 399–439.
Wallinga, J., Murray, A.S., Wintle, A.G., 2000. The single-aliquot regenerative-dose (SAR) protocol applied to coarse-grain feldspar. Radiat. Meas. 32, 529–533.
Watanabe, H., 1998. Comprehensive List of Tsunamis to Hit the Japanese Islands [second Edition]. University of Tokyo Press, Tokyo 238pp.
Wintle, A.G., 1973. Anomalous fading of thermoluminescence in mineral samples. Nature 245, 143–144.